




# Electrosound and asymmetry of the I–V characteristic induced by ultrasound in the $\text{Re}_x\text{Mn}_{1-x}\text{S}$ ( $\text{Re} = \text{Tm}, \text{Yb}$ )

Sergey Aplesnin<sup>1,2</sup>, Maxim Sitnikov<sup>2</sup>, Oxana Romanova<sup>1</sup>, Anton Kharkov<sup>2,a</sup> , Olga Begisheva<sup>2</sup>, Fyodor Zelenov<sup>2</sup>

<sup>1</sup> Kirensky Institute of Physics, Federal Research Center KSC SB RAS, Krasnoyarsk, Russia 660036

<sup>2</sup> Reshetnev Siberian State University of Science and Technology, Krasnoyarsk, Russia 660037

Received: 22 May 2021 / Accepted: 30 January 2022

© The Author(s), under exclusive licence to Società Italiana di Fisica and Springer-Verlag GmbH Germany, part of Springer Nature 2022

**Abstract** A correlation between the temperatures corresponding to the maxima of the sound attenuation and temperature resistance coefficient in the  $\text{Re}_x\text{Mn}_{1-x}\text{S}$  solid solutions related to the condensation of electrons and holes has been established. X-ray diffraction, energy-dispersive X-ray spectrum, and scanning electron microscope techniques have been used to investigate the microstructure of the samples. In the  $\text{Yb}_{0.2}\text{Mn}_{0.8}\text{S}$  compound, a decrease in the ultrasound attenuation with increasing temperature has been observed. The functional dependences of the electrosound on the ultrasound intensity and carrier type and the change in the electrosound sign with temperature have been established. The asymmetry of the I–V characteristic depending on the ultrasound intensity and the attenuation coefficient depending on the electric field has been found. The nonlinear attenuation of the ultrasound as a function of the intensity has been observed. Model of elastic and inelastic scattering of current carriers by acoustic phonons, deformation interaction is used to explain the asymmetry.

## 1 Introduction

The effect of ultrasound on carrier transport and the effect of the current on the sound attenuation are important for both fundamental research and application. Ultrasound is used in semiconductors for preventing charge carrier recombination and to achieve a higher efficiency in the field of photocatalysis [1] and heterolaser frequency tuning under the action of ultrasonic waves [2, 3]. Ultrasound can be used to lift the degenerate states of the angular magnetic moment of holes [4]. The charge transport regulation under ultrasound in silicon at ultrahigh frequency was carried out in multilayer structures fabricated on a ZnO layer sandwiched between two  $\text{SiO}_2$  layers on top of a Si substrate [5]. The electron–electron correlations due to Coulomb interactions were investigated by acoustoelectric current through quasi-one-dimensional channels formed in an  $\text{Al}_x\text{Ga}_{1-x}\text{As}/\text{GaAsAl}_x\text{Ga}_{1-x}\text{As}/\text{GaAs}$  heterostructure [6]. The influence of ultrasonic loading on the diode effect based on the Schottky barrier was investigated in  $\text{Mo}/n-n^+-\text{Si}$  structures by current–voltage characteristics. The reverse current in the I–V characteristic increases to 60% under the action of ultrasound. It has been found that dominant charge transfer mechanisms are the thermionic emission at high temperature and the phonon-assisted tunneling at low temperature. The ultrasound loading affects both processes due to the decrease of Schottky barrier height and binding energy of the electron in the trap [7, 8].

The electromechanical characteristics of semiconductors with the piezoelectric properties are used in data processing. The optical and electrical properties are modulated by lattice straining, which leads to the change in the piezoelectric field [9, 10]. Charge transfer by acoustic phonons was examined on the  $(\text{Al}, \text{Ga})\text{As}/\text{GaAs}$  heterostructure in [11, 12]. The enhancement of the ultrasound current occurs via a decrease in the depth of potential wells. The growth of the conductivity weakens the effect of current on the ultrasound velocity.

The interaction of conduction electrons with acoustic phonons is governed by the intensity of an acoustic wave, and the nonlinear effects were observed at lower sound intensities, as compared with the elastic nonlinearity [13, 14]. In this case, the sound attenuation is different from the exponential dependence and acoustic waves can be amplified [15–17]. In sufficiently strong electric fields, the drift velocity of electrons can exceed its critical value (comparable with the speed of sound); then, the acoustic absorption coefficient changes its sign, i.e., the absorption is changed for the amplification [18]. The amplification of sound by the drift of carriers in piezoelectric semiconductors is of special interest due to the large value of the interaction of electrons with the sound. The piezoelectric fields of surface acoustic waves can be strong enough to form electron stripes [19, 20] and induce the electrosound via the dragging of conduction electrons by a traveling acoustic wave. At low sound intensities, the acoustoelectric current is proportional to the intensity; at high sound intensities, it becomes dependent on the intensity in a more complex way. It seems the most promising to use of the acoustoelectric current for studying the interaction of the elastic lattice vibrations with carriers, in particular, to determine the sign of carriers.

<sup>a</sup> e-mail: [khark.anton@mail.ru](mailto:khark.anton@mail.ru) (corresponding author)

In electron-doped semiconductors, a random potential with localized electrons is formed. The sound absorption is determined by the interaction of localized electrons with an acoustic wave below the percolation level and with conduction electrons above it [21]. The propagation of sound leads to the lattice strain and to the additional interaction of electrons with the strain field. Under the dynamic deformation, a weak longitudinal electric field is induced, which interacts with both localized and delocalized electrons. The acoustic wave is accompanied by a longitudinal wave of the effective field with potential  $U$  acting on electrons. The electrically inhomogeneous semiconductors without inversion centers in local areas can exhibit the piezoelectric effect [22, 23]. In such semiconductors, the strain induces electric fields, which can be much stronger than the strain field. Then, the absorption of sound by electrons in piezoelectric semiconductors can be several times stronger than the lattice absorption.

The strong interaction of electrons with the elastic subsystem can be implemented in sulfides of variable-valence rare-earth elements [24]. When the ytterbium ion changes its valence, its radius decreases, which leads to the strong deformation interaction. In the vicinity of clusters with rare-earth elements at the interface of Re–Mn ions, the inversion center is absent and a local piezoelectric effect is predetermined. The manganese ion spin coupled with the rare-earth ion spin via the exchange interaction is reduced [25, 26]. The localization of electrons and holes can give rise to a charge density wave; the transition temperature can be determined from the ultrasound attenuation [27].

The aim of this study is to find the critical temperatures of localization of electrons and holes in the solid solutions, establish the effect of sound on the asymmetry of the I–V characteristic (the diode effect) and sound attenuation upon variation in an external electric field, and determine the regions of linear and nonlinear acoustoelectric effects, including the electrosound in bulk semiconductors.

## 2 Results and discussion

The  $\text{Re}_x\text{Mn}_{1-x}\text{S}$  crystals were grown by melt crystallization of powdered sulfides with a purity of no worse than 99.9% in glassy carbon crucibles and a quartz reactor in the argon atmosphere using  $\text{NH}_4\text{CNS}$  as a sulfiding agent. The synthesis was carried out in two stages: heating the mixture to 500 °C with exposure at this temperature for 1 h and repeated sulfiding at 750–800 °C for 3 h after grinding. For the completeness of sulfiding and homogenization of the obtained powder sulfide, it was annealed at 800 °C for 30 h in the sulfiding atmosphere with repeated grinding of sulfides. The sulfidation completeness was controlled by X-ray diffractometry and weight control.

The melt crystallization was performed by high-frequency heating of a graphite crucible filled with 6–7 g of the sulfide powder. A quartz reactor with the crucible was moved through a single-turn inductor. The inert atmosphere in the reactor was maintained with argon. To obtain a sulfide melt, the desired parameters of the power supplied to the inductor were experimentally determined. The received crystals of the cylindrical form had the sizes  $10 \times 30$  mm, the weight about 6 g. From crystals, the tablets were prepared for research of properties.

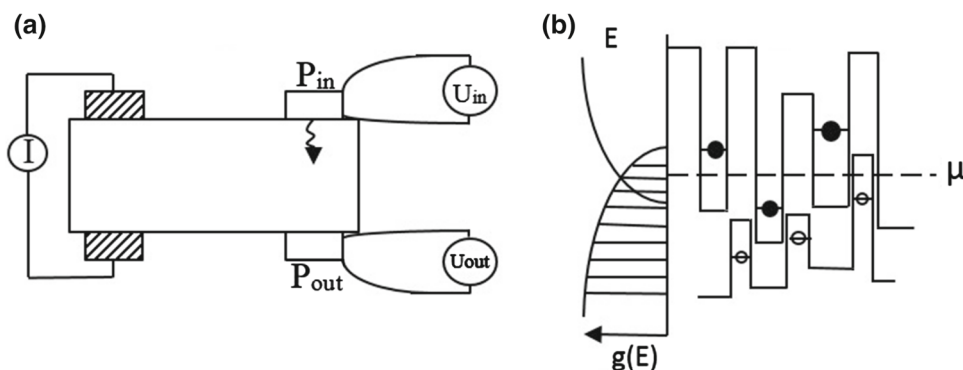
The interaction between the current and ultrasound was investigated on a rectangular sample  $8 \times 5 \times 4$  mm in size with current contacts on its opposite faces and two TsTS-19 piezoelectric sensors 4 mm in diameter (Fig. 1) with a distance of  $l = 4$  mm between them. A rectangular pulse with a length of 100 ns and 50 ns and a frequency of 1 MHz was supplied to one of the piezosensors and a voltage on the other sensor was detected. The ultrasound attenuation coefficient was determined from the ratio of the amplitudes of input voltage  $U_{\text{in}}$  and output voltage  $U_{\text{out}}$  of the piezosensors:

$$\alpha = \ln(U_{\text{in}}/U_{\text{out}})/l \quad (1)$$

The I–V characteristic of the  $\text{Re}_x\text{Mn}_{1-x}\text{S}$  samples was measured on a 2470 Keithley device.

The X-ray diffraction analysis of the  $\text{Re}_x\text{Mn}_{1-x}\text{S}$  samples was carried out on a DRON3 diffractometer ( $\text{CuK}\alpha$ -radiation) at room temperature. In the X-ray diffraction patterns of the solid solutions, diffraction reflections of a NaCl-type cubic structure are split into two; as an example, the main [200] peak is shown in Fig. 2a (inset). Possibly, the chemical pressure causes the formation of two

**Fig. 1** **a** Measurement scheme and **b** electron density of states  $g(E)$  near chemical potential  $\mu$



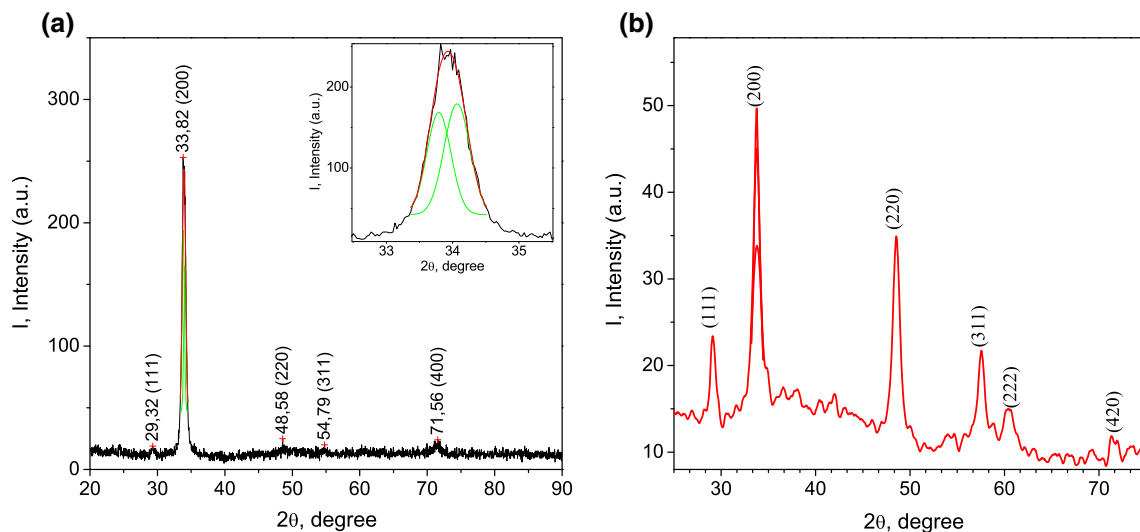


**Fig. 2** X-ray diffraction patterns of **a** the  $\text{Mn}_{0.9}\text{Tm}_{0.1}\text{S}$  and **b**  $\text{Mn}_{0.8}\text{Yb}_{0.2}\text{S}$  solid solutions

structures with an fcc lattice with the lattice constants different by  $\Delta a/a$  (0.7%). If the concentration of rare-earth ions is higher than the atomic percolation concentration in the lattice ( $X_c = 0.17$ ), then the intensity of the peaks decreases by an order of magnitude and the splitting vanishes (Fig. 2b).

The morphology of the samples  $\text{Tm}_{0.1}\text{Mn}_{0.9}\text{S}$  and  $\text{Yb}_{0.2}\text{Mn}_{0.8}\text{S}$  was studied by SEM Hitachi SU3500/Model 3500 SEM; high-resolution electron microscope Hitachi S-5500. SEM images were taken from  $982 \times$  to  $35,000 \times$  magnifications with acceleration voltage of 20 kV, and images of samples surface are shown in Fig. 3a and b. No granules are observed on the surface of the samples at a scale of 200 nm. From the SEM micrographs, samples are best interpret as single crystals. According to SEM data, from fitting the calculated spectrum to the experimental spectrum the degree of proximity to the ideal fcc structure in the space group  $Fm\bar{3}m$  (225) for  $\text{Tm}_{0.1}\text{Mn}_{0.9}\text{S}$  is 97.5% and for  $\text{Yb}_{0.2}\text{Mn}_{0.8}\text{S}$  is 89.5%. The elemental analysis of the samples  $\text{Tm}_{0.1}\text{Mn}_{0.9}\text{S}$  (Fig. 4a) and  $\text{Yb}_{0.2}\text{Mn}_{0.8}\text{S}$  (Fig. 4b) was performed by the energy-dispersive X-ray spectroscopy (EDS or EDX). The EDS spectrum and tables confirm the presence of thulium (Tm), sulfur (S), and manganese (Mn) in the sample  $\text{Tm}_{0.1}\text{Mn}_{0.9}\text{S}$  (Table 1) and of elements ytterbium (Yb), sulfur (S), and manganese (Mn) in the sample  $\text{Yb}_{0.2}\text{Mn}_{0.8}\text{S}$  (Table 2). Sulfur stoichiometry is satisfied with an accuracy of tenths of a percent. SEM images shows homogeneous distribution of elements in samples. The microstructure analysis indicate the good quality of the synthesized samples  $\text{Tm}_{0.1}\text{Mn}_{0.9}\text{S}$  and  $\text{Yb}_{0.2}\text{Mn}_{0.8}\text{S}$ .

In MnS, there exist structural rhombic lattice distortions at 165 K and rhombohedral distortions at 125 K, which are accompanied by a change in the lattice volume [28–30]. Substitution of ytterbium ions for manganese at a concentration of  $x = 0.05$  shifts the temperature of the phase transition from 125 to 105 K [31]. In the region of the structural phase transitions, the sound attenuation coefficient is maximum and related to the density fluctuations in the material [32]. The structural transitions in the  $\text{Mn}_{0.95}\text{Yb}_{0.05}\text{S}$  compound at 162 K and at low temperatures (102–110 K), which manifest themselves as kinks in the thermal expansion coefficient [31], give rise to the sound attenuation maxima (Fig. 5). Pinning of lattice polarons at the interface of Mn–Yb clusters at 450 K leads to the dynamic Jahn–Teller effect and to an increase in the lattice volume due to the electron compressibility [33]. The lattice strain induces a small anomaly in the sound attenuation coefficient and coincides in temperature with the temperature resistance coefficient  $(dR/dT) 1/T$  [34]. At 228 K, the resistance abruptly increases by a factor of 7 and is accompanied by the sound absorption maximum and the absence of anomalies in the thermal expansion coefficient. This is apparently due to the ordering of anionic vacancies in the anionic subsystem with the formation of a dipole glass, which leads to the absorption of sound.

Above this temperature, the correlation of vacancies decreases upon heating. Annealing in an external electric field of 600 V/cm for 5 min induces the ordering of charged vacancies. After switching-off the field, the attenuation logarithmically increases as  $\alpha/\alpha_0 = V_s \log(t)$  and reaches the saturation (Fig. 6). The relaxation rate  $V_s$  decreases upon heating. The time dependence of the sound attenuation is characteristic of glassy states [35, 36]. The linear growth of the sound attenuation coefficient upon heating above 330 K is caused by the polaron scattering on phonons according to the expression [37]:

$$(\alpha/f^2)_{\text{th}} = \frac{4\pi^2 \langle \gamma_i^j \rangle 2KT}{2\rho V^5} \quad (2)$$

where  $f$  is the phonon frequency,  $V$  is the phonon velocity,  $\rho$  is the phonon density,  $K$  is the thermal conductivity, and  $\gamma$  is the Gruziner parameter.

If the concentration  $x = 0.2$  is higher than the percolation concentration  $x_c = 0.17$ , then there exist macro regions larger than the sound wavelength that determine the ultrasound absorption. As was established from the PFY–XAS spectra [38], the  $f$  level position

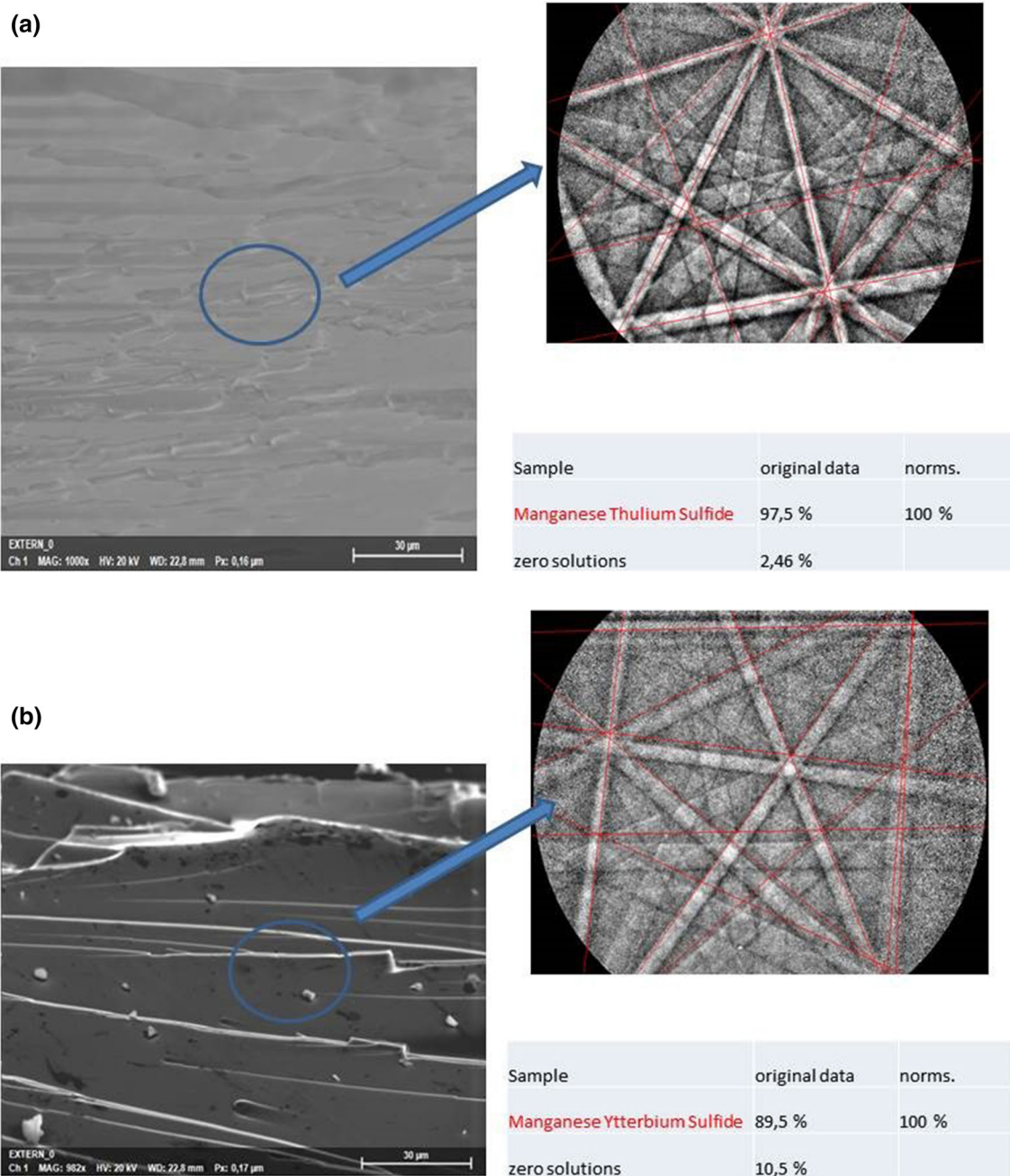


**Fig. 3** XRD&SEM image of samples  $\text{Tm}_{0.1}\text{Mn}_{0.9}\text{S}$  **a** and  $\text{Yb}_{0.2}\text{Mn}_{0.8}\text{S}$  **b**

relative to the bottom of the conduction band is lower than the Fermi level in YbS by 0.2 eV. The  $4f - 5d_{2g}$  hybridization of states in the vicinity of the  $X$  band point was found. Without pressure, the valence of ytterbium ions is  $\text{Yb}^{+2.1}$  and, at low pressures, it increases linearly due to the shift of the  $f$  level toward the  $d$  band. Due to the sound-induced pressure, a droplet is compressed and the electron density of states in the  $5d_{2g}$  subband changes. The absorption coefficient remains almost invariable up to 240 K and, above 330 K, the temperature dependence  $\alpha(T) = \alpha_0 T \exp(E_a/kT)$  is described analogously to the resistance with a variable hopping length, where the activation energy  $E_a = 535 \text{ cm}^{-1}$  is determined by the octahedra mode with a frequency of  $\omega = 518 \text{ cm}^{-1}$ . The small  $\alpha(T)$  anomalies at 165 K and 220 K coincide in temperature with the temperature resistance coefficient and are related to the lattice strain.

The switched-on ultrasound induces the asymmetry of the I–V characteristic and the diode effect above room temperature (Fig. 7). The I–V characteristic is nonlinear and obeys the power law  $I = AU^n$ , where  $n = 1.26$ . The power law dependence of current on voltage is characteristic of electrically inhomogeneous semiconductors. In the temperature range where charge ordering is observed,



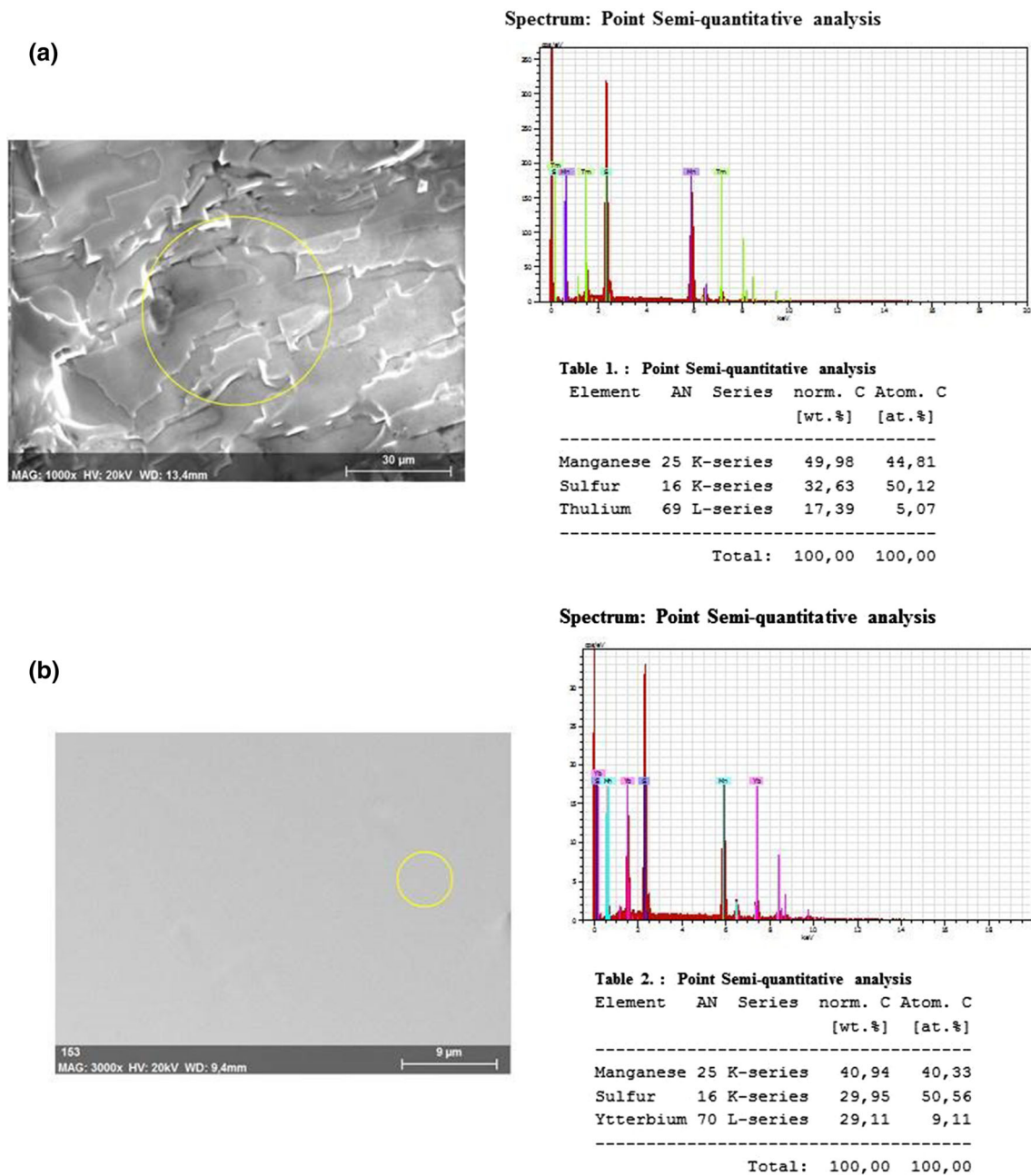


**Fig. 4** SEM image and EDS (spectrum and table) surface of the part of sample  $\text{Tm}_{0.1}\text{Mn}_{0.9}\text{S}$  **a** and  $\text{Yb}_{0.2}\text{Mn}_{0.8}\text{S}$  **b**

the conductivity is described in a model of currents limited by the space charge and is described by the quadratic Mott law [39–41]. The I–V hysteresis is not observed (inset in Fig. 7a). The decrease in current with increasing sound intensity above room temperature is caused by the interaction of current carriers with acoustic phonons induced by the piezoelectric sensor (Fig. 7b). If the direction of the current coincides with the direction of the phonon flux, then the probability of electron-phonon collisions decreases. In the case of oppositely directed impulses of electrons and phonons, the scattering increases, and the current decreases. This leads to an asymmetry of the I–V characteristic, which reaches  $\Delta I/I = (I(U = 10 \text{ V})/I(U = -10 \text{ V}) - 1) \approx 0.03$  at  $T = 440 \text{ K}$  (inset in Fig. 7b).

The ultrasound attenuation increases nonlinearly with increasing electric field. Up to 240 K, the attenuation is related to the deformation potential and described by the function  $\alpha = aE^2$  (Fig. 8a). The elastic energy of the system is added with the energy of the deformation induced by the acoustic wave  $U^b = \lambda u_{\text{def}} + 4\pi d u_k$ , where  $\lambda$  is the deformation potential,  $u_{\text{def}}$  is the deformation tensor,  $d$  is the piezoelectric coefficient, and  $u_k$  is the deformation value [42]. As a result of the deformations, the chemical potential  $\mu$  shifts and the electron density  $N$  changes at the chemical potential, so the bulk modulus of elasticity is  $1/B = d\mu/dN$ . The energy is transferred from the elastic to electron system under the periodic lattice compression. The relative change in the ultrasound

**Table 1** Spectrum: point semi-quantitative analysis

Element	AN	Series	Norm. C (wt, %)	Atom. C (at, %)
Manganese	25	K-series	49.98	44.81
Sulfur	16	K-series	32.63	50.12
Thulium	69	L-series	17.39	5.07
		Total:	100.00	100.00

**Table 2** Spectrum: point semi-quantitative analysis

Element	AN	Series	Norm. C (wt, %)	Atom. C (at, %)
Manganese	25	K-series	40.94	40.33
Sulfur	16	K-series	29.95	50.56
Ytterbium	70	L-series	29.11	9.11
		Total:	100.00	100.00

**Fig. 5** Sound attenuation coefficient in  $\text{Yb}_x\text{Mn}_{1-x}\text{S}$  with (1)  $x = 0.2$  and (2)  $x = 0.05$  (left-hand axis) and temperature resistance coefficient at (3)  $x = 0.2$  and (4)  $x = 0.05$  (right-hand axis) as functions of temperature. Inset: thermal expansion coefficient at  $x = 0.2$

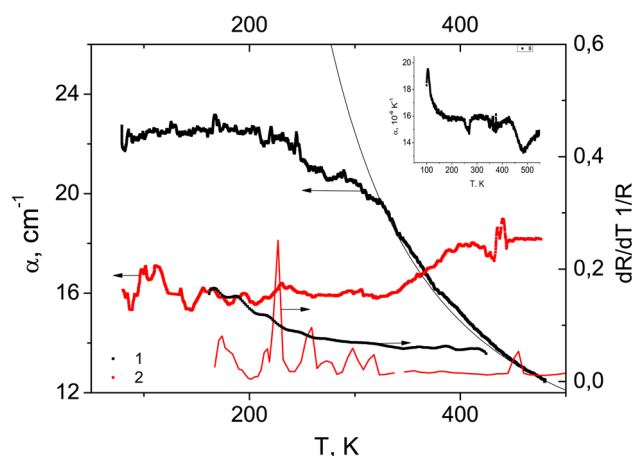
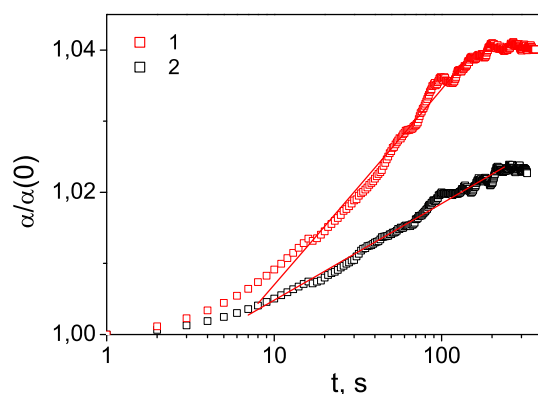


**Fig. 6** Relative change in the sound attenuation coefficient in  $\text{Yb}_{0.05}\text{Mn}_{0.95}\text{S}$  vs time after the action of an electric field of 600 V/cm for 5 min at temperatures of (1)  $T = 300$  K and (2)  $T = 330$  K



attenuation coefficient  $\Delta\alpha/\alpha$  in a maximum electric field (50 and 100 V) has a maximum at 200 and 280 K (Fig. 8b). At 270 K, the thermal expansion coefficient has a minimum (inset in Fig. 5).

In the range of 320–460 K, the field dependence of the attenuation coefficient becomes asymmetric relative to zero and the attenuation coefficient is added with a linear contribution. This contribution is related to the resonance interaction of the electron velocities with the speed of sound. The equation for the attenuation is [16]:

$$\alpha = \frac{K^2}{2} \frac{\omega_C}{(v_S - \mu E)} \left[ 1 + \frac{\omega_{CS}^2}{(v_S - \mu E)^2 \omega^2} \left( 1 + \frac{\omega^2}{\omega_C \omega_D} \right) \right]^{-1} \quad (3)$$

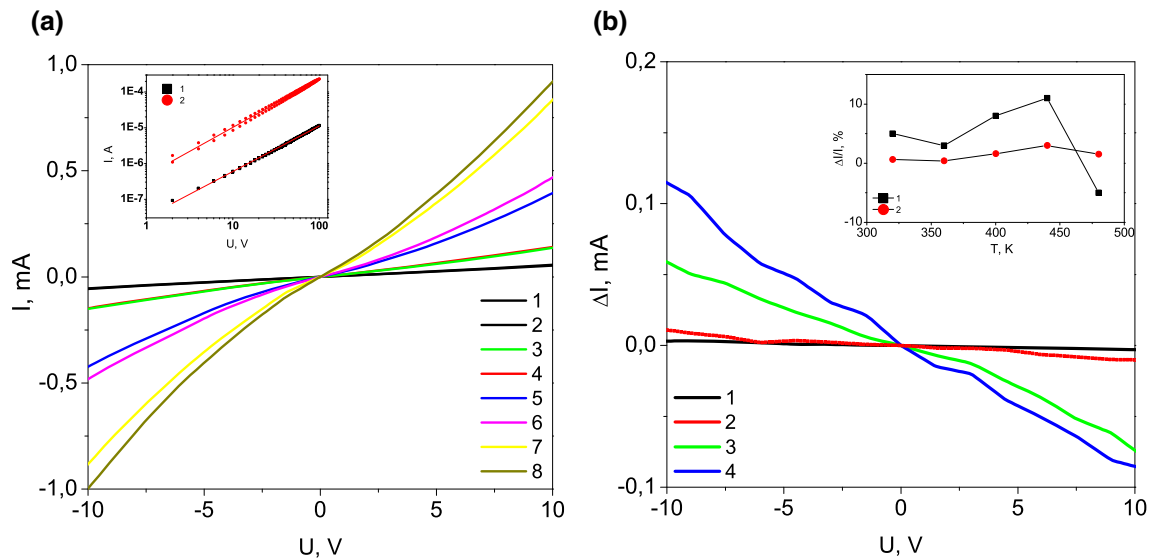


**Fig. 7** **a**  $I$ - $V$  characteristic for Yb<sub>0.2</sub>Mn<sub>0.8</sub>S at a piezosensor voltage of (2, 4, 6, 8)  $U = 1$  V and (1, 3, 5, 7)  $U = 10$  V at temperatures of (1,2)  $T = 320$  K, (3, 4)  $T = 360$  K, (5, 6)  $T = 400$  K, (7, 8)  $T = 440$  K. **b** Change in the current  $I(U = 10 \text{ V}) - I(U = 1 \text{ V})$  upon voltage variation at different sound intensities and (1)  $T = 320$  K, (2)  $T = 360$  K, (3)  $T = 400$  K, (4)  $T = 440$  K. Insets: **a**  $I$ - $V$  characteristic in the logarithmic coordinates at (1)  $T = 160$  K and (2)  $T = 240$  K, relative current variation (1)  $\Delta I/I = (I(U = 10 \text{ V})/I(U = 1 \text{ V}) - 1)$  and **b** asymmetry (2)  $\Delta I/I = (I(U = 10 \text{ V})/I(U = -10 \text{ V}) - 1)$  at a piezosensor voltage of  $U = 10$  V as functions of temperature

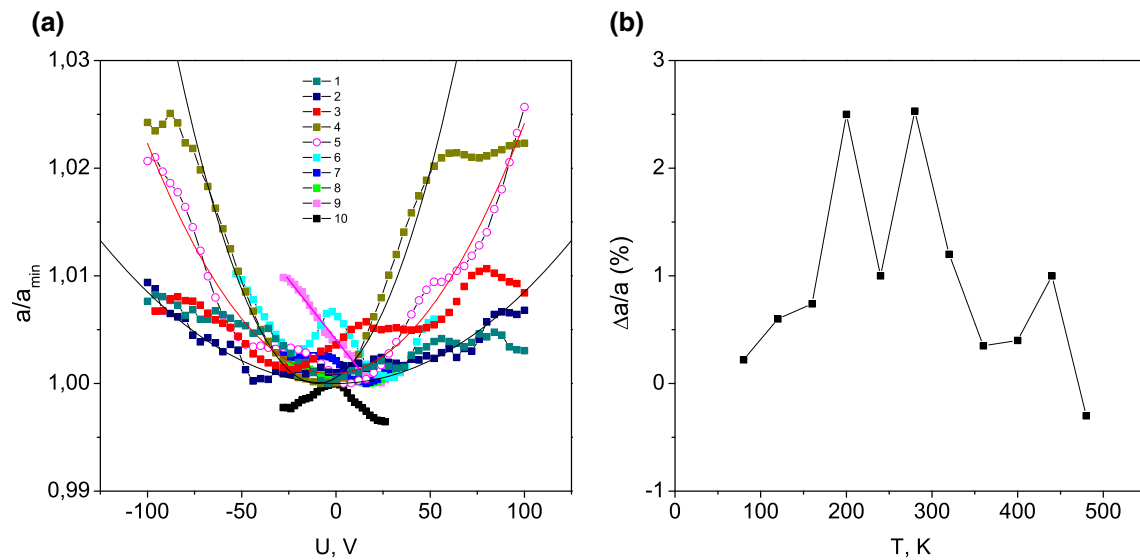
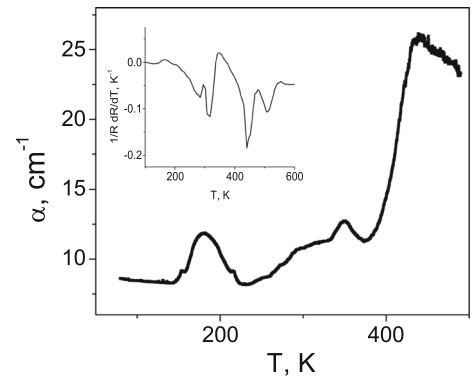


**Fig. 8** **a** Normalized ultrasound attenuation coefficient in the Yb<sub>0.2</sub>Mn<sub>0.8</sub>S solid solution at a piezosensor voltage of  $U = 10$  V as a function of voltage at temperatures of (1)  $T = 80$  K, (2)  $T = 120$  K, (3)  $T = 160$  K, (4)  $T = 200$  K, (5)  $T = 280$  K, (6)  $T = 320$  K, (7)  $T = 360$  K, (8)  $T = 400$  K, (9)  $T = 440$  K, (10)  $T = 480$  K. **b** Relative variation in the ultrasound attenuation coefficient  $\Delta a/a$  as a function of temperature in maximum electric fields (50 V and 100 V)

where  $K$  is the electromechanical coupling coefficient,  $\mu$  is the electron mobility,  $v_s$  is the speed of sound,  $E$  is the applied electric field,  $\omega_D$  is the acoustic frequency,  $\omega_c$  is the dielectric relaxation frequency, and  $\omega_D$  is the dielectric diffusion frequency. The coefficient  $\alpha$  is positive at the acoustic attenuation frequencies and negative at the acoustic amplification frequencies.

In our case, the inequality  $\omega \gg \omega_D$  is valid and, at  $v_s \gg \mu E$ , the expression is reduced to the form  $\alpha \sim \omega_c^2/\omega_D v_s (1 + \mu E/3v_s)$  and the normalized value  $\alpha(E)/\alpha(0) = 1 + \mu E/3v_s$ ,  $\lambda U \sim \beta E^2$  satisfactorily describes the experiment with  $\mu/3v_s \sim 10^{-4}$  and a mobility of  $0.01 \text{ cm}^2/\text{sV}$ , which is consistent with the data found by the Hall effect measurements. The presence of two contributions of the

**Fig. 9** Ultrasound attenuation coefficient of the  $\text{Tm}_{0.1}\text{Mn}_{0.9}\text{S}$  solid solution as a function of temperature. Inset: temperature resistance coefficient and thermoelectric power as a function of temperature



deformation (quadratic in the field) and resonance interactions causes the attenuation asymmetry  $\alpha(E)/\alpha(0) = 1 + AE + BE^2$  at the change in the external electric field polarity. The solution to the quadratic equation is:

$$E_{1,2} = \frac{(-A \pm \sqrt{A^2 - 4B})}{2B} = \frac{\mu}{6\beta v_s} \pm \frac{\sqrt{\left(\frac{\mu}{3v_s}\right)^2 + 4\beta}}{2\beta} \quad (4)$$

where  $\beta$  is the coefficient of electrostriction. In a strong electric field, electrons are delocalized and the lattice is compressed, i.e.,  $B = -\beta$ , and  $\beta$  is taken modulo in formula (4). At  $T = 320$  K, the normalized value  $\alpha(E)/\alpha(0)$  has two minima at  $U_1 = -20$  V and  $U_2 = 28$  V. With an increase in temperature, instead of one of the minima, a shoulder forms and one minimum remains at 30 V. Perhaps this is due to an increase in the mobility of charge carriers. According to SEM data and X-ray diffraction, the sample has a highly symmetric cubic structure and the change in volume at 480 K is caused by the electronic transition (insert in Fig. 5). At 480 K, the thermal expansion coefficient has a minimum caused by the disappearance of charge ordering and an increase in the lattice volume. Possibly, at this temperature, the electron density fluctuations are suppressed by the electric field, which leads to a decrease in the sound attenuation with increasing electric field.

In the  $\text{Tm}_{0.1}\text{Mn}_{0.9}\text{S}$  solid solution, the sound attenuation coefficient has several maxima at temperatures of 178, 290, 350, 442 K (Fig. 9). The temperature of the first maximum coincides with the temperature of the local maximum of the electrical resistance; the rest temperatures are consistent with the temperatures of extrema in the temperature dependence of the electrical resistance at 285, 348, and 440 K (inset in Fig. 9) [43]. At 180 K, there is an IR mode intensity anomaly at  $3110 \text{ cm}^{-1}$ . The pirocurrent has a broad maximum in the temperature range of 250–325 K [44]. Delocalization of electrons in the range of 420–450 K leads to a relative decrease in the sample volume, which was found from the thermal expansion coefficient. Anomalies in the temperature dependence of the electrical resistance and in the linear sizes of the sample are caused by the electron compressibility [45].

For the  $\text{Tm}_{0.1}\text{Mn}_{0.9}\text{S}$  solid solution, we investigate the effect of the sound intensity on the conductivity and the effect of the electric field on the sound attenuation. Figure 10 shows the I–V characteristics, which are nonlinear in weak electric fields. As the sound intensity increases, the resistance decreases, except for the temperature range of 180–200 K with the maximum sound attenuation. The maximum change in the current upon variation in the sound intensity is obtained at 120–200 K (20–30%) and above room temperature (10%), where  $\Delta I = (I_2 - I_1)/I_1$  with  $I_2, I_1$  corresponding to the current at the voltage amplitude from  $U_2 = 10$  V and  $U_1 = 1$  V on the piezosensor (inset in Fig. 10c). The asymmetry of the I–V characteristic (the diode effect) is maximum (3% and 8%) at 160 and 400 K (inset in Fig. 10d).

The sound attenuation coefficient increases in an electric field (Fig. 11) and has a positive value. When the polarity of the external electric field is reversed, the symmetry is not observed, except for a temperature of 320 K. At the small acoustic wave amplitude, the attenuation minimum is observed in zero field. With an increase in the sound intensity, the dependence of the attenuation coefficient on the external field weakens and, at low temperatures, the  $\Delta\alpha/\alpha$  minimum shifts toward positive fields. Possibly, in this temperature range, a piezoelectric contribution from the interface between Re–Mn clusters is added and the attenuation minimum is obtained in this field. The existence of areas with electric polarization is confirmed by the high dielectric constant  $\epsilon = 175$  in  $\text{Tm}_{0.1}\text{Mn}_{0.9}\text{S}$  at room temperature [44]. The electric field of Tm–Mn clusters is partially screened by free charge carriers. Under the action of ultrasound the binding energy of the hole with cluster decreases and the concentration of current carriers at the chemical potential level increases with an increase in the ultrasound intensity. The asymmetry of the I–V characteristic arises as a result of deformation interaction  $\sim aE^2$  and inelastic interaction of electrons (holes) with acoustic phonons. On the opposite faces of the sample, a gradient of lattice polarons is created, which transfer the charge and lead to the formation of an electric potential difference (Up). The voltage depending on the ultrasound intensity is given in inset of Fig. 12.

The type of carriers is determined from the electroacoustic: these are the carriers dragged by the phonon flux. In Fig. 12, the electroacoustic changes its sign from positive to negative at a temperature of 340 K. At this temperature, the ultrasound attenuation in the  $\text{Tm}_{0.1}\text{Mn}_{0.9}\text{S}$  solid solution has a maximum. With increasing temperature, the current increases. In the  $\text{Yb}_{0.2}\text{Mn}_{0.8}\text{S}$  solid



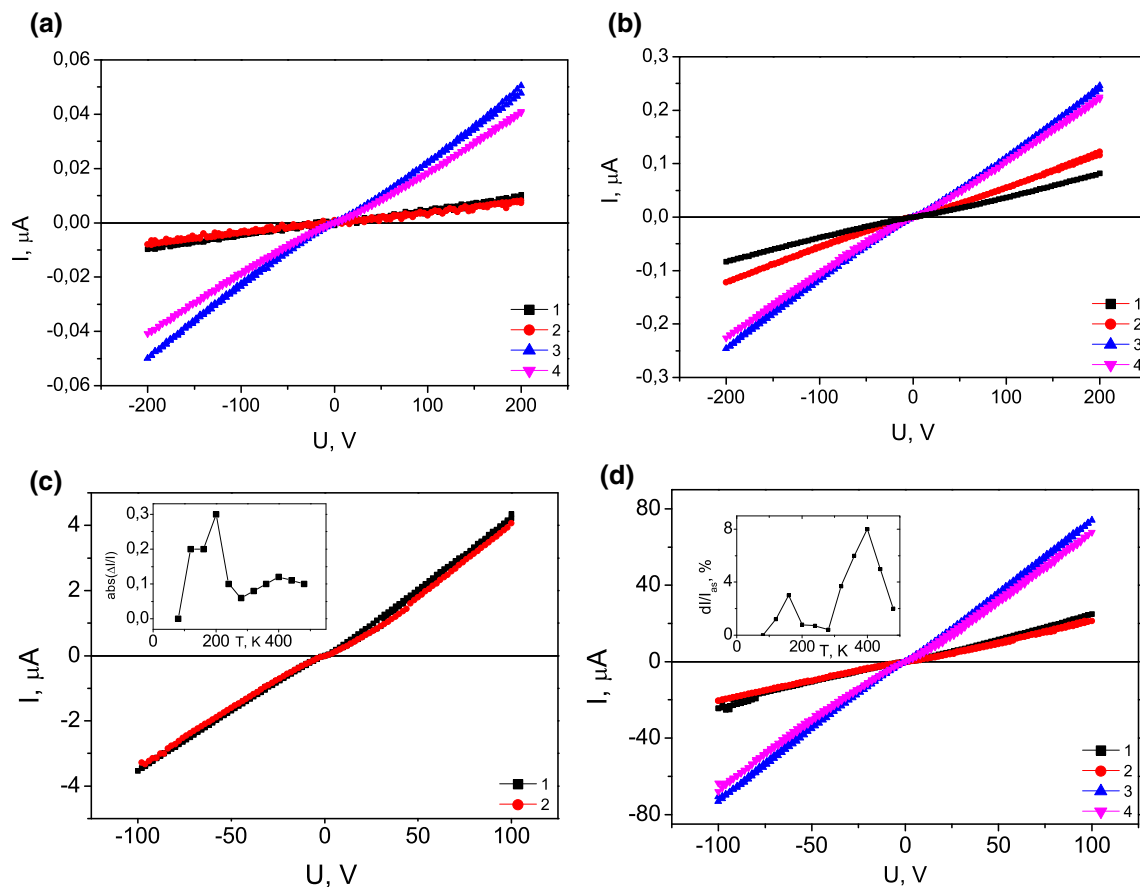


**Fig. 10** I–V characteristic of the  $\text{Tm}_{0.1}\text{Mn}_{0.9}\text{S}$  solid solution at a piezosensor voltage of **a** (1, 3)  $U = 10$  V and (2, 4)  $U = 1$  V at temperatures of (1,2)  $T = 120$  K and (3, 4)  $T = 160$  K, **b** (1, 2)  $U = 200$  V and (3, 4)  $U = 240$  V. **c** (1, 2)  $U = 320$  V, and **d** (1,2)  $U = 400$  V and (3, 4)  $U = 480$  V. Insets: **d** relative current variation  $\Delta I/I = (I(U = 10 \text{ V})/I(U = 1 \text{ V}) - 1)$  at a piezosensor voltage of  $U = 10$  V as a function of temperature

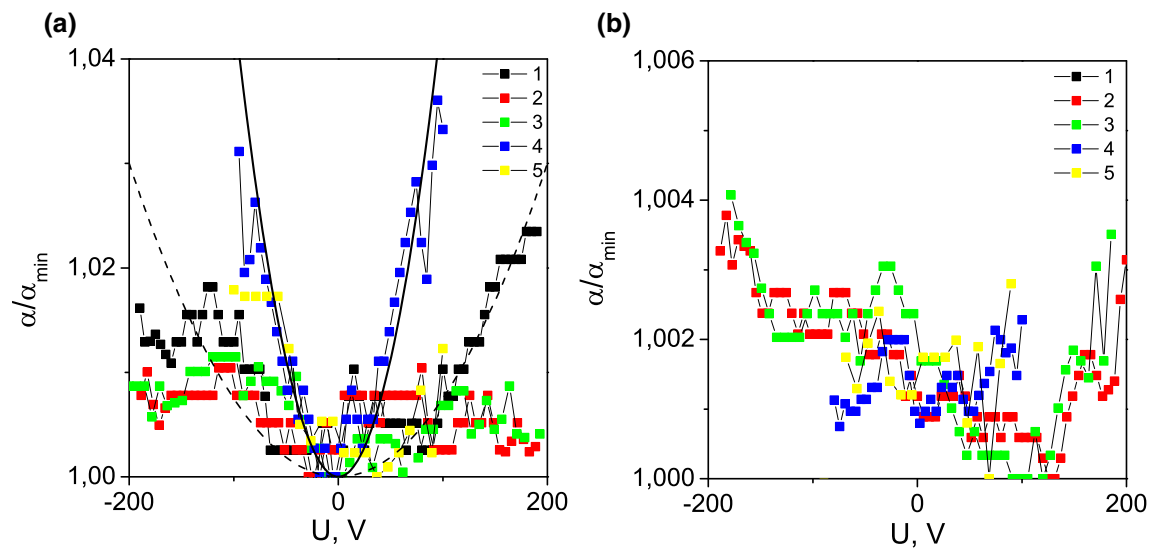


**Fig. 11** Normalized ultrasound attenuation coefficient of the  $\text{Tm}_{0.1}\text{Mn}_{0.9}\text{S}$  solid solution at a piezosensor voltage of **a**  $U = 10$  V and **b**  $U = 1$  V as a function of voltage at temperatures of (1)  $T = 120$  K, (2)  $T = 160$  K, (3)  $T = 240$  K, (4)  $T = 320$  K, (5)  $T = 400$  K

solution, the electrosound also increases upon heating and passes through a maximum at 350 K. In the range of 350–375 K, the electrosound changes its sign with increasing sound intensity.

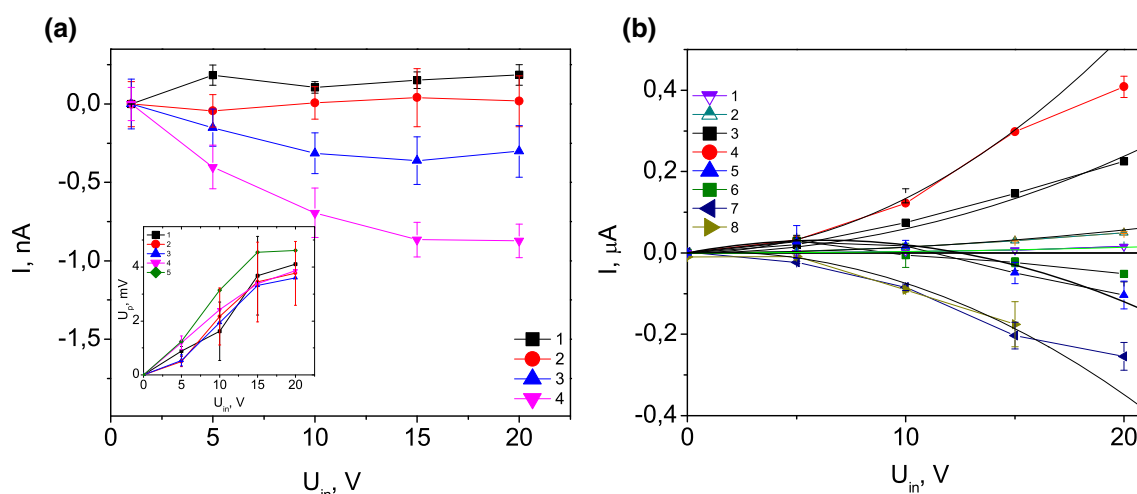


**Fig. 12** Electroacoustic in **a**  $\text{Tm}_{0.1}\text{Mn}_{0.9}\text{S}$  at (1)  $T = 300$  K, (2)  $T = 340$  K, (3)  $T = 380$  K, (4)  $T = 420$  K, and **b**  $\text{Yb}_{0.2}\text{Mn}_{0.8}\text{S}$  at (1)  $T = 200$  K, (2)  $T = 250$  K, (3)  $T = 300$  K, (4)  $T = 350$  K, (5)  $T = 375$  K, (6)  $T = 400$  K, (7)  $T = 440$  K, (8)  $T = 480$  K as a function of the piezosensor voltage. Fitting functions  $I = AU_{\text{in}}(BU_{\text{in}} - 1)$  (solid lines) with  $A = 0.4$  (3),  $A = 1$  (4),  $B = 32$  (a);  $A = 0.005$ ,  $B = 12$  (3),  $A = 0.01$ ,  $B = 13.5$  (4),  $A = -0.01$ ,  $B = 0.1$  (7) (b). Inset: the voltage created by the ultrasound versus intensity

We explain the observed effects using the model with a random potential and electron(hole) hoppings over the strained potential wells (Fig. 1b). In the temperature range of 340–70 K, the chemical potential shifts from the region of potential wells with holes to potential wells with electrons. This leads to a change in the spectral density of electron states and to overlapping of tails at the chemical potential level (Fig. 1b).

At the low sound intensity, the acoustoelectric current density  $j(S)$  is related to the absorption coefficient  $\alpha$  by the Weinreich relation [46]:

$$j = \frac{\sigma \alpha S}{en v_s} \quad (5)$$

where  $\sigma$  is the conductivity,  $S$  is the intensity,  $n$  is the electron density, and  $v_s$  is the speed of sound. This relation follows from the energy and quasi momentum conservation laws at the interaction of an acoustic wave with conduction electrons. In semiconductors with two types of carriers the electroacoustic is determined by the flux of phonons that drag electrons and holes. In the  $\text{Tm}_{0.1}\text{Mn}_{0.9}\text{S}$  solid solution electroacoustic  $j = 0$  at 340 K and the hole and electron concentrations are equal. Above this temperature, the electroacoustic are approximated by a nonlinear function of the intensity  $I = AU_{\text{in}}(BU_{\text{in}} - 1)$  with prevail an electron current carriers.

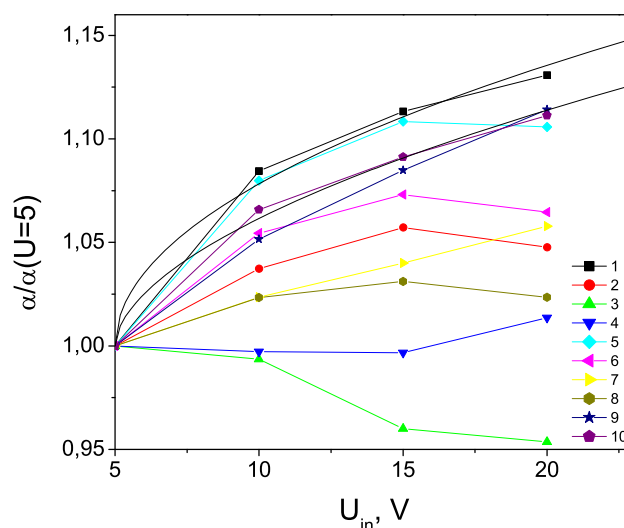
In  $\text{Yb}_{0.2}\text{Mn}_{0.8}\text{S}$ , the electroacoustic is determined by the hole concentration in the temperature range of 200–350 K. At temperatures of 375–425 K, the electroacoustic changes its sign and a carrier type; in particular, at  $T > 440$  K, the electron hole-type carriers prevail.

Figure 13 shows the sound attenuation as a function of intensity for the  $\text{Tm}_{0.1}\text{Mn}_{0.9}\text{S}$  solid solution. In the magnetically ordered region and above 400 K, the attenuation coefficient increases according to the power law:  $\alpha \sim AU_{\text{in}}^n$ ,  $n < 1$ . This is possibly due to the transfer of energy to the current carriers and to the magnetic subsystem as result of the magnetoelastic interaction at 80 K. In the temperature range of 120–360 K, the sound attenuation coefficient decreases at the input piezoelectric sensor voltages above 15 V with an increase in the sound intensity.

### 3 Conclusion

The XRD analysis and SEM image confirm the cubic structure in space group  $Fm\bar{3}m$  (225) of the samples. EDS confirms the presence of elements in the sample, homogeneity and stoichiometry. The maxima of the ultrasound attenuation were found in the vicinity of the rhombohedral lattice distortion and electron localization. At the concentrations, below the percolation value, the sound attenuation increases upon heating above 300 K and decreases in the  $\text{Yb}_{0.2}\text{Mn}_{0.8}\text{S}$  compound when ytterbium ions percolation over the lattice. The asymmetry of the  $I$ - $V$  characteristic (the diode effect) in  $\text{Re}_x\text{Mn}_{1-x}\text{S}$  depending on the electric field direction and the speed of ultrasound was found. In  $\text{Yb}_x\text{Mn}_{1-x}\text{S}$ , the asymmetry is due to the elasticity of the interaction of current carriers with longitudinal acoustic phonons, in  $\text{Tm}_x\text{Mn}_{1-x}\text{S}$  by the dragging of electrons by phonons. An increase in the current in  $\text{Tm}_x\text{Mn}_{1-x}\text{S}$  is due to decrease of the binding energy of the hole with polar cluster (trap) and a decrease in the current in  $\text{Yb}_x\text{Mn}_{1-x}\text{S}$  with elasticity scattering on phonons. The asymmetry of sound attenuation caused by deformation interaction and interaction with current carriers is found. In the  $\text{Re}_x\text{Mn}_{1-x}\text{S}$  solid solutions, the critical temperature related to a change in the electroacoustic sign was found. It was demonstrated that the current carriers concentration on the chemical level depends on the sound intensity. The correlation of the temperatures resistance coefficient and local maxima of the sound attenuation, and the thermal expansion coefficient was established.

**Fig. 13** Ultrasound attenuation coefficient  $\alpha$  normalized to  $\alpha(U = 5 \text{ V})$  at (1)  $T = 80 \text{ K}$ , (2)  $T = 120 \text{ K}$ , (3)  $T = 160 \text{ K}$ , (4)  $T = 200 \text{ K}$ , (5)  $T = 240 \text{ K}$ , (6)  $T = 280 \text{ K}$ , (7)  $T = 320 \text{ K}$ , (8)  $T = 360 \text{ K}$ , (9)  $T = 400 \text{ K}$ , (10)  $T = 440 \text{ K}$  as a function of the input piezosensor in  $\text{Tm}_{0.1}\text{Mn}_{0.9}\text{S}$ . Fitting function of the attenuation coefficient  $\alpha = 1 + A\sqrt{(U_{\text{in}} - 5)}$  with  $A = 0.035(1)$ ,  $A = 0.025(10)$  (solid line)



**Acknowledgements** This study was supported by the Russian Foundation for Basic Research and the Belarusian Republic Foundation for Basic Research (Project No. 20-52-00005). The investigation of microstructural properties of the samples was carried out using equipment's (SEM and TEM) the Krasnoyarsk Regional Center of Research Equipment of Federal Research Center «Krasnoyarsk Science Center SB RAS». The authors are grateful to A.V. Shabanov, senior researcher of the Laboratory of Molecular Spectroscopy, Kirensky Institute of Physics, for the scanning electron microscopy investigations.

**Data Availability Statement** This manuscript has no associated data or the data will not be deposited. [Authors' comment: The data that support the findings of this study are available from the corresponding author upon reasonable request.]

## References

1. R. Vinoth, P. Karthik et al., *Phys. Chem. Chem. Phys.* **18**, 5179 (2016). <https://doi.org/10.1039/C5CP08041J>
2. L.A. Kulakova, I.S. Tarasov, *JETP Lett.* **78**, 67 (2003). <https://doi.org/10.1134/1.1615531>
3. L.A. Kulakova, V. Gorelov et al., *Sol. St. Commun.* **152**, 1690 (2012). <https://doi.org/10.1016/j.ssc.2012.04.065>
4. I.V. Rozhansky, M.B. Lifshits et al., *Phys. Rev. B* **80**, 085314 (2009). <https://doi.org/10.1103/PhysRevB.80.085314>
5. S. Buyukkose, B. Vratzov et al., *J. Appl. Phys. Lett.* **102**, 013112 (2013). <https://doi.org/10.1063/1.4774388>
6. J.H. He, J. Gao, H.Z. Guo, *J. Appl. Phys. Lett.* **97**, 122107 (2010). <https://doi.org/10.1063/1.3491287>
7. O. Oliikh, K. Voytenko, *Ultrasonics* **66**, 1 (2016). <https://doi.org/10.1016/j.ultras.2015.12.001>
8. O. Oliikh et al., *J. Semicond.* **37**, 122002 (2016). <https://doi.org/10.1088/1674-4926/37/12/122002>
9. C. Rocke, S. Zimmermann et al., *Phys. Rev. Lett.* **78**, 4099 (1997). <https://doi.org/10.1103/PhysRevLett.78.4099>
10. M. Streibl, A. Wixforth et al., *Appl. Phys. Lett.* **75**, 4139 (1999). <https://doi.org/10.1063/1.125562>
11. M.J. Hoskins, H. Morko, B.J. Hunsinger, *Appl. Phys. Lett.* **41**, 332 (1982). <https://doi.org/10.1063/1.93526>
12. W.J. Tanski, S.W. Merritt, R.N. Sacks et al., *Appl. Phys. Lett.* **52**, 18 (1988). <https://doi.org/10.1093/IJEDM.1987.191582>
13. V.I. Pustovoit, *UFN* **97**, 257 (1969). <https://doi.org/10.3367/UFNr.0097.196902c.0257>
14. Yu.M. Galperin, V.L. Gurevich, V.I. Kozub, *UFN* **128**, 107 (1979). <https://doi.org/10.3367/UFNr.0128.197905d.0107>
15. Yu. Gulyaev, F.S. Hickernell, *Acoust. Phys.* **5**, 81 (2005). <https://doi.org/10.1134/1.1851632>
16. R.W. Smith, *Phys. Rev. Lett.* **9**, 87 (1962). <https://doi.org/10.1103/PhysRevLett.9.87>
17. S.K. Abdelraheem, D.P. Blyth, N. Balkan, *Phys. Stat. Sol. A* **185**, 247 (2001). [https://doi.org/10.1002/1521-396X\(200106\)185:2%3c247::AID-PSSA247%3e3.0.CO;2-H](https://doi.org/10.1002/1521-396X(200106)185:2%3c247::AID-PSSA247%3e3.0.CO;2-H)
18. S.Y. Mensah, N.G. Mensah et al., *Phys. E* **28**, 500 (2005). <https://doi.org/10.1016/j.physe.2005.05.050>
19. G. Weinreich, T.M. Sanders, H.G. White, *Phys. Rev.* **114**, 33 (1959). <https://doi.org/10.1103/PhysRev.114.33>
20. M. Rotter, A.V. Kalameitsev et al., *Phys. Rev. Lett.* **82**, 2171 (1999). <https://doi.org/10.1103/PHYSREVLETT.82.2171>
21. L. Wang, S. Liu et al., *Nat. Nanotech.* **15**, 661 (2020). <https://doi.org/10.1038/s41565-020-0700-y>
22. M.M. Yang, Z.D. Luo et al., *Nature* **584**, 377 (2020). <https://doi.org/10.1038/s41586-020-2602-4>
23. L. Peters et al., *Phys. Rev. B* **92**, 035143 (2015). <https://doi.org/10.1103/PhysRevB.92.035143>
24. A. Wixforth, *Phys. Rev.* **3**, 14 (1999). <https://physics.aps.org/story/v3/st14>
25. S.S. Aplesnin, A.M. Kharkov et al., *JMMM* **352**, 1 (2014). <https://doi.org/10.1016/j.jmmm.2013.09.061>
26. S.S. Aplesnin, A.M. Kharkov et al., *JMMM* **347**, 10 (2013). <https://doi.org/10.1016/j.jmmm.2013.07.044>
27. G. Benedek et al., *J. Phys. Chem. Lett.* **11**, 1927 (2020). <https://doi.org/10.1021/acs.jpclett.9b03829>
28. H.H. Heikens, C.F. van Bruggen, C.J. Haas, *Phys. Chem. Sol.* **39**, 833 (1978). [https://doi.org/10.1016/0022-3697\(78\)90141-5](https://doi.org/10.1016/0022-3697(78)90141-5)
29. G.A. Petrakovskii, S.S. Aplesnin et al., *Phys. Sol. St.* **33**, 406 (1991)
30. S.S. Aplesnin, G.A. Petrakovskii et al., *Sol. St. Commun.* **129**, 195 (2004). <https://doi.org/10.1016/j.ssc.2003.09.028>
31. S.S. Aplesnin, A.M. Kharkov et al., *Bull. Rus. Acad. Sci. Phys.* **77**, 1252 (2013). <https://doi.org/10.3103/S1062873813100031>
32. L.V. Udod, S.S. Aplesnin et al., *J. Alloys Compd.* **804**, 281 (2019). <https://doi.org/10.1016/j.jallcom.2019.07.020>
33. S.S. Aplesnin, M.N. Sitnikov et al., *JMMM* **513**, 167104 (2020). <https://doi.org/10.1016/j.jmmm.2020.167104>
34. S.S. Aplesnin, O.B. Romanova et al., *Phys. Sol. St.* **57**, 886 (2015). <https://doi.org/10.1134/S1063783415050029>
35. I.Y. Korenblit, E.F. Shender, *Sov. Phys. Usp.* **32**, 139 (1989). <https://doi.org/10.3367/UFNr.0157.198902b.0267>

36. S.S. Aplesnin, L.V. Udod et al., Mater. Res. Exp. **5**, 115202 (2018). <https://doi.org/10.1088/2053-1591/aaddd9>
37. S.K. Kor, R.R. Yadav, J. Phys. Soc. Jpn. **55**, 207 (1986). <https://doi.org/10.1143/JPSJ.55.207>
38. I. Jarrige, H. Yamaoka et al., Phys. Rev. B **87**, 115107 (2013). <https://doi.org/10.1103/PhysRevB.87.115107>
39. N.F. Mott, E.F. Davis, *Electronic Processes in Non-Crystalline Materials* (Oxford, N. Y., 1971)
40. B.I. Shklovskii, A.L. Efros, *Electronic Properties of Doped Semiconductors* (Science, Moscow, 1979)
41. B.I. Shklovskii, A.L. Efros, Sov. Phys. Usp. **18**, 845 (1975). <https://doi.org/10.1070/PU1975v018n11ABEH005233>
42. Yu.M. Galperin, V.L. Gurevich, V.I. Kozub, Sov. Phys. Usp. **22**, 352 (1979). <https://doi.org/10.1070/PU1979v022n05ABEH005499>
43. S.S. Aplesnin, O.B. Romanova et al., Phys. Sol. St. **58**, 19 (2016). <https://doi.org/10.1134/S1063783416010029>
44. S.S. Aplesnin, M.N. Sitnikov et al., Phys. Stat. Sol. B **256**, 1900043 (2019). <https://doi.org/10.1002/pssb.201900043>
45. S.S. Aplesnin, A.M. Kharkov, GYu. Filipson, Phys. Stat. Sol. B **257**, 1900637 (2020). <https://doi.org/10.1002/pssb.201900637>
46. G. Weinreich, Phys. Rev. **107**, 317 (1957). <https://doi.org/10.1103/PhysRev.107.317.2>